Kaneshima and Matsuzawa *Progress in Earth and Planetary Science* (2015) 2:15
DOI 10.1186/s40645-015-0046-5

Progress in Earth and Planetary Science
a SpringerOpen Journal

RESEARCH ARTICLE Open Access

Stratification of earth's outermost core inferred from SmKS array data

Satoshi Kaneshima[1*] and Takanori Matsuzawa[2]

Abstract

S*m*KS arrivals recorded by large-scale broadband seismometer arrays are analyzed to investigate the depth profile of P wave speed (V_p) in the outermost core. The V_p structure of the upper 700 km of the outer core has been determined using S*m*KS waves of Fiji-Tonga events recorded at stations in Europe. According to a recent outer core model (KHOMC), the V_p value is 0.45 % slower at the core mantle boundary (CMB) than produced by the Preliminary Reference Earth Model (PREM), and the slow anomaly gradually diminishes to insignificant values at ~300 km below the CMB. In this study, after verifying these KHOMC features, we show that the differential travel times measured for S*m*KS waves that are recorded by other large-scale arrays sampling laterally different regions are well matched by KHOMC. We also show that KHOMC precisely fits the observed relative slowness values between S2KS, S3KS, and S4KS (S*m*KS waves with $m = 2$, 3, and 4). Based on these observations, we conclude that S*m*KS predominantly reflect the outer core structure. Then we evaluate biases of secondary importance which may be caused by mantle heterogeneity. The KHOMC V_p profile can be characterized by a significant difference in the radial V_p gradient between the shallower 300 km and the deeper part of the upper 700 km of the core. The shallower part has a V_p gradient of $-0.0018\ s^{-1}$, which is steeper by $0.0001\ s^{-1}$ when compared to the deeper core presented by PREM. The steeper V_p gradient anomaly of the uppermost core corresponds to a radial variation in the pressure derivative of the bulk modulus, $K' = dK/dP$. The K' value is 3.7, which is larger by about 0.2 than that of the deeper core. The radial variation in K' is too large to have a purely thermal origin, according to recent ab initio calculations on liquid iron alloys, and thus requires a thick and compositionally stratified layering at the outermost outer core.

Keywords: Outermost core; Compositional stratification; S*m*KS waves; Array processing

Background

Stratification of the outermost core has been long suspected (e.g., Lay and Young 1990; Buffett and Seagle 2010) and has been recently strongly advocated by Helffrich and Kaneshima (2010) and Kaneshima and Helffrich (2013) (respectively abbreviated as HK2010 and KH2013 hereafter). The present study consolidates the propositions of HK2010 and KH2013 by investigating additional S*m*KS data obtained for significantly more event-array pairs and by evaluating possible mantle effects on S*m*KS travel time and slowness observations. We analyze S*m*KS arrivals with integer m from 2 to 5 in order to better constrain the V_p profile of the topmost 700 km of the core, anticipating that the results will strengthen the evidence for a compositionally stratified layer. As shown in Fig. 1, the ray paths of S2KS, S3KS, and S4KS propagate quite a long distance through the outermost part of the core. Since each S*m*KS possesses a distinct depth sensitivity depending both on m and epicentral distance, when used in combination, S*m*KS waves can form an ideal data set for use in determining the V_p profile of the outermost core. In order to measure differential travel time and slowness differences between two S*m*KS waves, we used large-scale broadband seismometer arrays in Europe, Eastern Asia (including Japan), North and South America, Africa, and Australia.

Prior to HK2010 and KH2013, other studies also investigated the outer core structure by analyzing S*m*KS data. The proposed models show either slightly or rather strongly slower V_p anomaly relative to the Preliminary Reference Earth Model (PREM) (Dziewonski and Anderson 1981) near the top of the core. For instance,

*Correspondence: kane@geo.kyushu-u.ac.jp
[1] Department of Earth and Planetary Science, Kyushu University, Hakozaki, Higashi-ku, 812-8581 Fukuoka, Fukuoka, Japan
Full list of author information is available at the end of the article

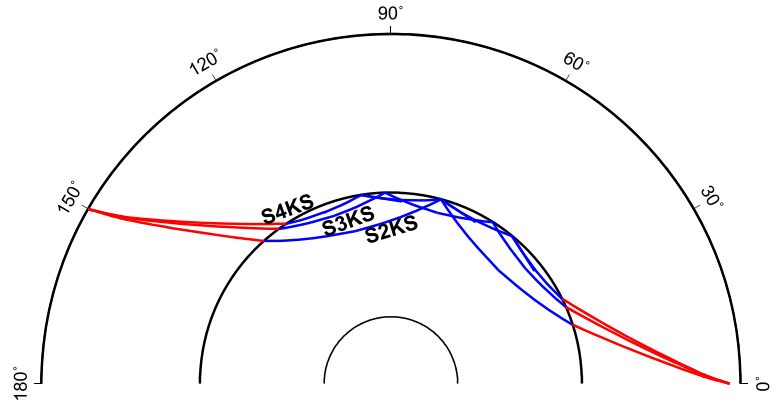

Fig. 1 S*m*KS ray paths. Ray paths of S*m*KS waves (S2KS, S3KS, and S4KS) propagating through the outermost part of the core to a receiver at a epicentral distance of 150°. Blue and red lines show P and S wave portions of the rays, respectively

Tanaka (2007) analyzed a composite record section of S2KS, S3KS, and S4KS, which were observed globally, and proposed a model with up to a maximum of 1.2 % slower V_p than PREM in the outermost 90 km of the core. His model (called Tanaka-1 hereafter) is similar to that presented in an earlier study by Garnero et al. (1993). Alexandrakis and Eaton (2010) investigated composite globally observed record sections of S2KS to S4KS for the distance range shorter than 140° and showed a permissible range of V_p profiles for the top 200 km of the outer core. The range of permissible models centers around slightly slower V_p values (from ∼0.1 to 0.4 %) than PREM and falls between PREM and the IASP91 velocity model (Kennett and Engdahl 1991). In this study, we also include other global V_p models such as SP6 (Morelli and Dziewonski 2012), AK135 (Kennett et al. 1995), and another model proposed by Tanaka (2007) (called Tanaka-3 hereafter) with the models to be compared.

S*m*KS waveform data

S*m*KS data are analyzed for earthquakes that occurred in several different regions and were recorded at large-scale broadband stations prior to July 2014 (Table 1). The broadband seismograms in Europe are extracted from the Incorporated Research Institutions for Seismology (IRIS) and the Observatories and Research Facilities for European Seismology (ORFEUS) data management centers. Seismic stations in Japan belong to J-Array, F-net, and the tilt-meter network of Hi-net (Obara et al. 2005). Data of the seismic stations in Eastern Asia outside of Japan, the US, and Australia are extracted from the IRIS data management center (DMC). In this study, we loosely define a "large-scale array" as a group of 20 or more broadband seismometer stations with aperture lengths exceeding ∼1000 km whose seismograms can be analyzed by standard array processing methods. As we shall show later, travel times of S*m*KS waves observed at individual stations may be significantly affected by the heterogeneous mantle structure, rather irrespective of the waveform quality. This makes it difficult to investigate a detailed V_p profile of the outer core based on S*m*KS measurements made for individual traces. However, HK2010 and KH2013 showed that stacking seismograms over an entire large-scale array substantially suppresses the mantle effects and thereby enables us to discern the fine structure of the outermost core. In this study, we shall also show that the processing of large-scale array data enables us to precisely retrieve differential slowness between two S*m*KS arrivals, which helps to better constrain the outer core structure. Figure 2 shows an example of observed and computed record sections for a Fiji-Tonga event recorded at the European stations. The synthetic seismograms shown in Fig. 2b are computed for PREM using reflectivity (Kind 1979) and a method similar to that of Wang et al. (2008) (HK2010). When S*m*KS touches an internal caustic and is underside reflected $m-1$ times at the core mantle boundary (CMB), it suffers from a phase delay by nearly $\frac{m-1}{2}\pi$ relative to SKS (Choy 1977). The arrivals of S2KS, S3KS, S4KS, S5KS, and S6KS are clearly visible on this section and are systematically delayed with respect to the theoretical PREM predictions throughout the array.

Methods and results

Array measurements

In this study, we measure differential travel times between two different S*m*KS waves on stacked waveforms; those between S3KS and S2KS (called dt^{3-2} hereafter), S4KS and S3KS (called dt^{4-3}), and S5KS and S3KS (called dt^{5-3}). Next, the differential time anomalies relative to the ray theoretical predictions based on PREM are computed. Since instrument corrections have negligible effects on the results, stacking and differential time measuring are performed directly on the observed broadband seismograms (HK2010). We also avoid unstable deconvolution of

Table 1 Event list

Event	Date	Time	Lat. N	Lon. E	h (km)	Mo (dyne cm)
FEV1	2007/10/05	7:17:52	−25.19	179.46	509	6.8×10^{25}
FEV2	2007/10/16	21: 5:43	−25.77	179.53	509	1.0×10^{26}
FEV3	2008/07/03	3: 2:37	−23.37	−179.78	581	2.8×10^{25}
FEV4	2011/07/29	7:42:24	−23.79	179.75	537.0	1.5×10^{26}
FEV5	2007/05/06	21:11:53	−19.40	−179.35	676	6.1×10^{25}
FEV6	2012/01/24	00:52: 5	−24.977	178.520	580.3	4.2×10^{25}
FEV7	2008/07/19	22:39:53	−17.337	−177.312	391.	5.2×10^{25}
FEV8	2011/08/19	3:54:27	−16.522	−177.004	407.9	2.9×10^{25}
FEV9	2008/10/19	5:10:34	−21.863	−173.819	29.0	2.9×10^{26}
FEV10	2009/03/19	18:17:41	−23.050	−174.660	34.0	3.4×10^{27}
FEV11	2009/11/24	12:47:16	−20.710	−174.040	18.0	1.7×10^{26}
FEV12	2014/07/21	14:54:41	−19.829	−178.464	616.	3.0×10^{26}
FEV13	1998/03/29	19:48:16	−17.552	−179.092	537.5	6.4×10^{26}
KEV1	2013/04/26	6:53:29	−28.68	−178.96	358.8	2.1×10^{25}
KEV2	2011/02/21	10:57:52	−26.142	178.394	558.0	7.9×10^{25}
KEV3	2007/09/25	5:16: 1	−30.965	179.998	417.	2.3×10^{25}
KEV4	2009/08/18	21:20:47	−26.064	−178.391	269.3	3.6×10^{25}
KEV5	2013/08/28	2:54:41	−27.75	179.62	480.3	2.9×10^{25}
KEV6	2014/06/23	19:19:16	−30.118	−177.67	20.	2.6×10^{26}
AEV1	2000/04/23	9:27:23	−28.31	−62.99	609	3.1×10^{26}
AEV2	2005/03/21	12:23:54	−24.98	−63.47	579	2.3×10^{26}
AEV3	2008/09/03	11:25:14	−26.74	−63.22	570	3.3×10^{25}
AEV4	2012/05/28	5: 7:24	−28.06	−63.11	589.3	1.3×10^{26}
AEV5	2011/09/02	13:47:11	−28.420	−63.150	592.8	1.4×10^{26}
AEV6	2014/04/03	1:58:30	−20.311	−70.576	24.1	9.6×10^{25}
NCEV	2014/04/11	20:29:12	11.642	−85.878	135.0	1.0×10^{25}
IEV1	2011/08/30	6:57:42	−6.36	126.76	469.0	2.7×10^{26}
IEV2	2010/03/20	14: 0:50	−3.36	152.24	414	9.2×10^{25}
IEV3	2010/07/23	22: 8:11	6.72	123.41	607.0	1.2×10^{27}
IEV4	2013/06/13	16:47:23	−10.0	107.24	9.0	1.1×10^{26}
IEV5	2011/03/10	17:08:37	−6.87	116.72	510.6	9.7×10^{25}
IEV6	2010/05/31	19:51:45	11.132	93.471	112.	6.4×10^{25}
MEV	2006/02/22	22:19: 8	−21.32	33.58	11	4.2×10^{26}
INEV	2008/05/31	4:37:56	−41.290	80.47	10.	5.1×10^{25}
SEV1	2014/06/29	7:52:56	−55.506	−28.451	16.5	2.4×10^{26}
PEV1	2013/05/14	0:32:26	18.728	145.287	602.3	2.1×10^{26}

the source time function, which may cause some biases to the dt^{m-n} (differential travel times between SmKS and SnKS waves) and their anomalies relative to ray theoretical predictions by PREM, which are usually positive. Those biases are mostly less than 0.2 s for the Fiji-Tonga events used in HK2010 and KH2013 but can be larger for other events. Therefore, we evaluate biases by using synthetic seismograms (Fig. 2b). To measure these synthetic seismograms dt^{m-n}, we use the same array method as the data and compare them with the theoretical ray calculations based on PREM. The difference, which is usually 0.2 to 0.3 s but sometimes could exceed 0.5 s (Table 2), is regarded as the bias. For each event, dt^{3-2} are measured both by picking peaks and cross-correlating the stacked waveforms after correcting for the $\frac{\pi}{2}$ phase shift due to the caustic (Choy 1977). Both S2KS and S3KS are

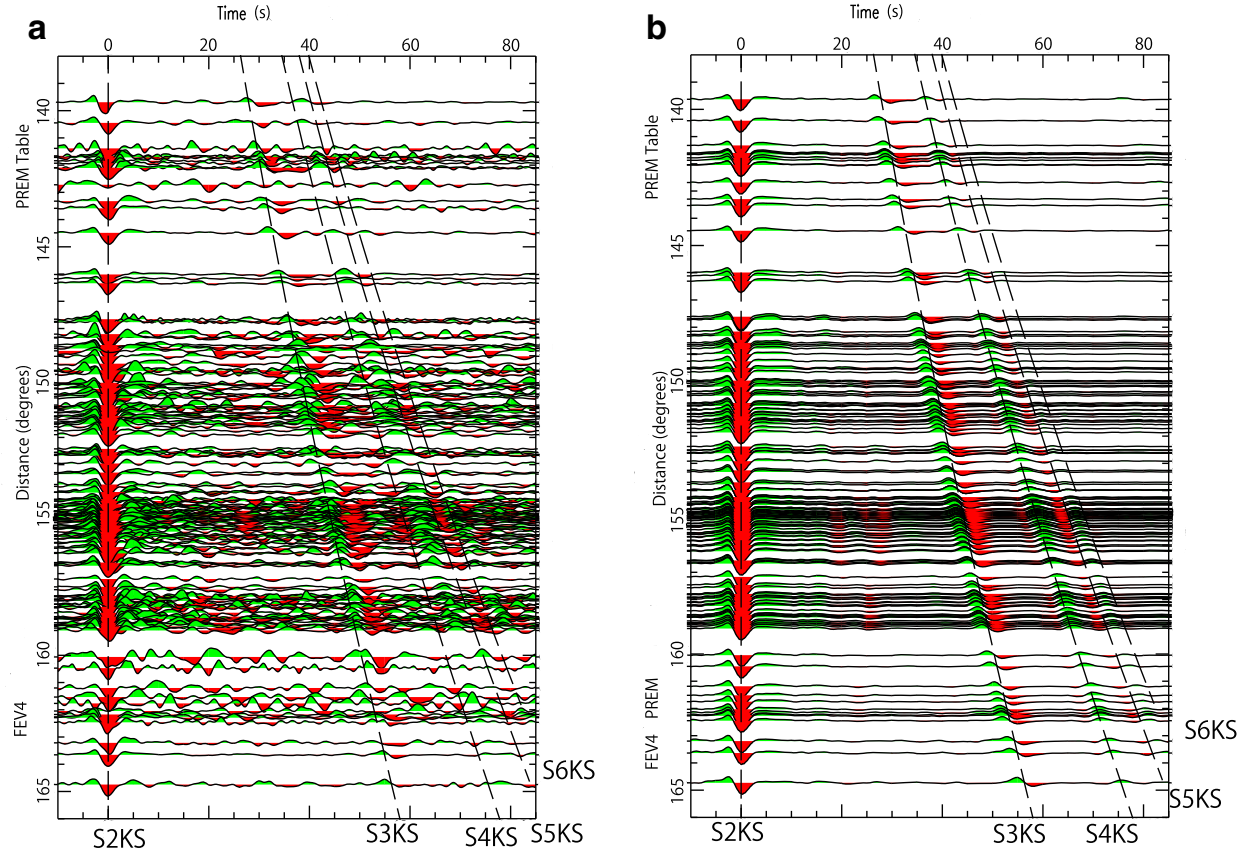

Fig. 2 Observed and synthetic record sections. The observed (**a**) and computed (**b**) record sections of a Fiji-Tonga event recorded at the European stations. The arrivals of S2KS, S3KS, S4KS, S5KS, and S6KS are clearly visible. When aligned on S3KS arrivals, S4KS and S5KS waves are systematically delayed relative to PREM across the entire array. In this example, dt^{3-2}, dt^{4-3}, and dt^{5-3} are anomalous by about +1.2 s

used as the alignment phase whenever the S3KS arrival is sufficiently clear, and the agreements between different alignment phases (S2KS or S3KS) and between different methods (peak-picking or cross correlating) are used for evaluating the error of each dt^{3-2} measurement. The measured differential times are classified into two categories, A (high quality) and B (moderate) (Table 2). When the values obtained by different methods agree with each other, the stacked synthetic and observed seismograms usually agree quite well, and the measurements can be regarded as category A, and have smaller errors.

In addition to the $\frac{\pi}{2}$ phase shift, waveforms of S4KS could be distorted by the interference by S5KS (Eaton and Kendall 2006) or by S3KS when epicentral distances are not large. The S5KS arrivals are not separated completely from S4KS, even when its peak, which is oppositely polarized to S3KS, can be clearly identified. Therefore, dt^{4-3} and dt^{5-3} are measured simply by identifying the corresponding peaks. Since alignment on S4KS arrivals is usually unstable, differential times between S4KS and S5KS (called dt^{5-4}) are calculated by subtracting dt^{4-3} from dt^{5-3} with error propagation. Other array measurement details are described in HK2010 and KH2013. We note that, especially for the Tonga-Fiji events (Fig. 2a), the anomalies of dt^{m-n} relative to PREM are observed more or less uniformly across the entire European array (KH2013). Except for the uniform delays, no systematic trends in the differential times with azimuth from the Tonga-Fiji events, which may be amenable to elaborate modeling, have been identified for the high quality events. This would suggest only minor influences of CMB structure on individual paths.

V_p model for the outermost core

$\tau - p$ inversion: effects of starting model

KH2013 built a V_p model of the topmost 700 km of the outer core using differential S*m*KS travel time anomalies of several Fiji-Tonga events recorded at Europe, dt^{3-2}, dt^{4-3}, and dt^{5-3}, to which a $\tau - p$ inversion method had been applied (Garmany et al. 1979; HK2010; KH2013), with PREM as the starting model. The resultant model, KHOMC, has a 0.45 % slower V_p than PREM at the CMB

Table 2 Differential travel times are measured on the waveforms which are obtained by linearly stacking the observed broadband seismograms with the relative slowness computed for PREM

Event	Array	Distance	dt^{3-2} (s)	Bias	dt^{4-3} (s)	Bias	dt^{5-3} (s)	Bias	Category
FEV1	EU	154.0	1.2 ± 0.2	0.1	1.0 ± 0.2	0.2	1.2 ± 0.3	0.2	A
FEV2	EU	154.0	1.1 ± 0.2	0.2	1.2 ± 0.2	0.2	1.2 ± 0.3	0.3	A
FEV3	EU	152.5	1.1 ± 0.3	0.1	1.3 ± 0.3	0.3	1.5 ± 0.4	0.2	A
FEV4	EU	152.	1.6 ± 0.2	0.2	1.3 ± 0.2	0.2	1.2 ± 0.3	0.3	A
FEV5	EU	147.3	1.5 ± 0.3	0.3	1.3 ± 0.4	0.2	1.6 ± 0.5	0.0	A
FEV6	EU	153.5	1.6 ± 0.4	0.2	0.9 ± 0.2	0.2	1.1 ± 0.4	0.1	A
FEV6	US	123.5	0.9 ± 0.3	0.3	-		-		B
FEV7	EU	148.5	1.5 ± 0.4	0.3	1.4 ± 0.3	0.4	1.3 ± 0.4	0.4	B
FEV8	EU	148.	1.1 ± 0.5	0.3	-		-		B
FEV9	EU	153.	1.2 ± 0.5	−0.1	-		-		B
FEV10	EU	151.9	0.9 ± 0.4	−0.3	-		-		B
FEV11	EU	151.9	1.1 ± 0.4	0.0	-		-		B
FEV12	EU	150.0	1.3 ± 0.2	0.3	1.2 ± 0.2	0.4	1.1 ± 0.3	0.3	A
FEV13	AF	131.	0.2 ± 0.3	−0.1	0.2 ± 0.2	−0.1	-		B
KEV1	EU	155.	1.2 ± 0.2	0.3	1.2 ± 0.3	0.4	1.0 ± 0.4	0.4	A
KEV2	EU	153.	1.9 ± 0.4	0.2	1.0 ± 0.3	0.2	-		B
KEV3	EU	155.	1.4 ± 0.4	0.2	-		-		B
KEV4	EU	155.	1.6 ± 0.5	0.4	1.5 ± -	0.4	-		B
KEV5	EU	155.5	1.2 ± 0.4	0.3	1.2 ± 0.4	0.2	1.5 ± 0.5	0.1	A
KEV6	EU	155.	1.4 ± 0.3	0.2	1.5 ± 0.5	0.3	-		B
AEV1	JP	162.4	0.5 ± 0.4	0.1	0.9 ± 0.4	0.2	-		B
AEV2	HI	157.8	0.9 ± 0.4	−0.1	1.3 ± 0.2	0.2	1.4 ± 0.3	−0.1	A
AEV3	HI	162.6	0.5 ± 0.5	0.0	0.9 ± 0.4	0.2	0.8 ± 0.5	0.2	B
AEV4	HI	160.0	0.6 ± 0.3	−0.1	0.6 ± 0.3	0.3	0.5 ± 0.3	0.2	A
AEV4	AU	124.8	0.7 ± 0.3	0.6	-		-		B
AEV4	AS	167.9	1.0 ± 0.4	0.0	-		-		B
AEV5	JP	163.4	1.0 ± 0.4	0.0	-		-		B
AEV5	AU	124.7	0.6 ± 0.4	0.4	-		-		B
AEV5	AS	167.8	1.0 ± 0.4	0.0	1.4 ± 0.5	0.6	-		B
AEV6	JP	153.9	0.6 ± 0.4	−0.1	-		-		B
NCEV	AU	140.1	2.0 ± 0.5	0.7	1.0 ± 0.5	0.3	-		B
IEV1	US	130.9	1.3 ± 0.4	0.2	-		-		B
IEV2	EU	122.8	0.9 ± 0.4	0.1	-		-		B
IEV2	US	119.5	0.9 ± 0.4	0.1	-		-		B
IEV3	US	120.9	0.8 ± 0.5	−0.4	-		-		B
IEV4	US	144.	1.0 ± 0.4	0.4	1.0 ± 0.5	0.4	0.9 ± 0.5	0.5	A
IEV5	US	141.	0.9 ± 0.3	0.1	0.3 ± 0.3	0.0	0.3 ± 0.5	0.2	A
IEV6	US	133.1	0.4 ± 0.2	0.2	0.1 ± 0.3	−0.2	-		B
MEV	US	149.2	1.0 ± 0.5	0.2	-		-		B
INEV	US	168.6	0.2 ± 0.5	−0.3	1.2 ± 0.4	0.5	-		B
SEV1	AK	154.1	0.4 ± 0.5	0.1	-		-		B
SEV1	JP	153.8	0.9 ± 0.3	0.2	-		-		A
PEV1	SA	149.5	1.9 ± 0.3	0.5	0.5 ± 0.5	0.6	-		B

Array distances correspond to approximate array centers, whose accurate value do not affect the results. The values of "Bias" are measured by applying the array method on the reflectivity seismograms computed for PREM and comparing the differential *SmKS* travel times with the ray theoretical predictions

(Fig. 3). The lower-than PREM V_p values persist down to about 300 km below the CMB. We note here that the $\tau - p$ method is a linear inversion that requires a good starting model. Although PREM is known to be a good global model, there may be other reference models as good as PREM. We perform the $\tau - p$ inversion using IASP91 as the starting model, as did Alexandrakis and Eaton (2010). By using only the Fiji-Tonga to European stations data, as in the case of KHOMC, we obtained a profile of V_p anomaly relative to IASP91 (called KOCTI). KOCTI has faster V_p values than IASP91 in the shallowest 300 km of the outer core (Fig. 3). KOCTI shows an improved fit to the data compared to IASP91 (Fig. 3), but its overall fit is less suitable than that of KHOMC, with the most significant disagreement for the dt^{3-2} data of larger distances, as will be shown later in this study. The V_p values of KOCTI for the upper 300 km are only about 0.01 km/s slower than those of KHOMC (the V_p at the CMB is −0.045 km/s relative to PREM, while that of KHOMC is −0.035 km/s). Therefore, it can be seen that the two models agree with each other within the uncertainty range (Fig. 3). We conclude that the V_p at CMB is constrained well by the $\tau - p$ inversion to 8.03 ± 0.01 km/s, irrespective of the starting model. The disagreement between KOCTI and KHOMC for the depth range from about 300 km to 700 km from the CMB is larger (by about −0.02 km/s), suggesting a poorer resolution than the shallower core.

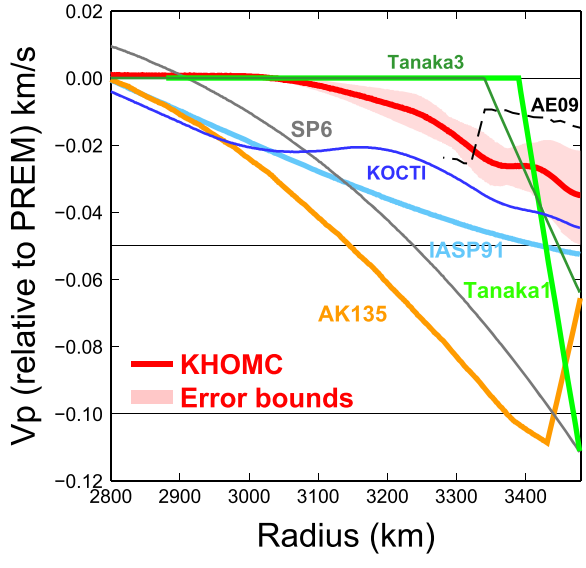

Fig. 3 V_p models of outermost core. V_p models of the upper 700 km of the outer core: KHOMC, AK135, SP6, Tanaka-1, Tanaka-3, IASP91, AE09 (Alexandrakis and Eaton 2010), and KOCTI. The V_p values (in km/s) as a function of depth relative to the PREM values are shown. The uncertainty range of KHOMC are shown in pink (KH2013)

Genetic algorithms

In order to check further the effects of the starting model on the result, we perform another V_p inversion using genetic algorithms (e.g., Yamanaka and Ishida 1995) and attempt to find the global minimum of dt^{m-n} misfit in a fashion that does not explicitly require a starting model. The V_p profile of the outer 700 km of the core is assumed to be continuous and consist of four layers with constant V_p gradients. For each layer, the V_p value at its top and its thickness are determined (see the caption of Fig. 4 for details).

We use the data set consisting of dt^{3-2}, dt^{4-3}, and dt^{5-4} data for four events from Fiji-Tonga to Europe (FEV1, FEV2, FEV3, FEV4) and three events from Argentina to

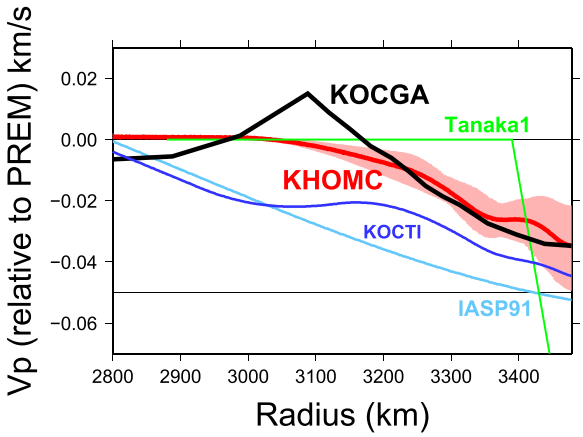

Fig. 4 Genetic algorithm. The V_p model obtained by the inversion using genetic algorithms. The thick black line labeled KOCGA is the obtained continuous V_p model of the outer 700 km of the core, which has four layers with uniform V_p gradients. Other details are the same as Fig. 3. The thickness of the deepest layer is fixed to 400 km and the V_p value at the bottom of the layer is fixed to that of PREM, so that there are seven parameters to be determined, each of which is described as a 6-bit binary number. Therefore, each gene has a length of 42 bits. The least bit for the V_p at the top of each layer corresponds to 0.003 km/s, while the least bit for the thickness corresponds to 2 km. The depth of the CMB is fixed to that of PREM, so the inversion is not entirely free from the reference model, but the effect is quite small insofar as the differential travel times of S*m*KS waves are concerned. The range of the V_p value sought by this parameterization covers about ±0.2 km/s relative to PREM, which is wide enough not to miss any successful models. First, the samples of V_p model of the first generation are constructed by randomly selecting the seven model parameters. Second, the misfit of the model predictions to the observations is computed, and each V_p model sample is selected with a probability proportional to the inverse of the squared sum of its misfit. After the selection, crossover of the genes between two randomly selected samples occurs with a given probability, followed by the mutation within each gene that occurs with a given probability, in order to generate the samples of the next generation. This process is iterated through the fixed number of generations. The total misfit over the entire samples usually converges rapidly enough. The parameters used in the inversion are as follows: both the mutation probability and the crossover probability are 0.2, and the numbers of sample and generation are 100 and 40, respectively

Japan (AEV1, AEV2, AEV3) without correcting for bias (Table 2). The inversion is repeated 40 times with different initial values, and the case with the least misfit, for which the total residual decreases from 0.5 to 0.15 s through the 40 generations, is chosen. As shown in Fig. 4, the obtained model (called "KOCGA" hereafter) is fairly close to KHOMC. The agreement between the model and KHOMC is remarkable especially for the shallower 300 km of modeled depth range. Based on this result, we conclude that the validity of KHOMC is not affected by the choice of the starting model.

S*m*KS slowness measurements

In addition to travel time differences, differences in slowness between two S*m*KS waves provide information on the relative arrival directions of the waves. In HK2010 and KH2013, it was reported that the relative slownesses for the Tonga and Argentina events are close to those predicted by PREM. This observation has been exploited in using the τ-p inversion. The slowness observations can also give constraints on the degree of large-scale heterogeneity in the receiver-side mantle, as shall be shown in the "Discussion" section. The differential slowness between two different S*m*KS waves changes gradually with distance. Therefore, the moveout of a S*m*SK wave, relative to the reference S*m*KS wave on a record section, is aligned on a slightly curved line rather than a straight line. Although the curvature is small, when the aperture of an array is as large as 20°, its effect on the differential travel times approaches a second, which could give rise to a small bias of the measured differential slowness between S*m*KS and S*n*KS relative to PREM (called "dp^{m-n}"). To ensure that dp^{m-n} is measured accurately, we correct for the curvature by assuming that the moveout around the array center (distance of Δ_0) is a quadratic function of epicentral distance when stacking seismograms. Accordingly, the differential slowness between S3KS and S2KS (and similarly between S4KS and S2KS) is expressed as

$$dp^{3-2}(\Delta) = dp^{3-2}(\Delta_0) + (\Delta - \Delta_0)\frac{d}{d\Delta}dp^{3-2}$$

The curvatures of the moveout curve are fixed to those of the reference model, so that $\frac{d}{d\Delta}dp$ is 0.014 and 0.021 s/$^{\circ 2}$ for dp^{3-2} and dp^{4-2}, respectively, which does not significantly affect the results. We obtain precise slowness measurements of S3KS and S4KS waves with S2KS as the reference wave for eight Fiji-Tonga and Kermadec events observed from Europe, and four Argentina events observed from Japan (Table 3). The dp^{3-2} and dp^{4-2} are then compared to the predictions of KHOMC (Table 3).

Figure 5a shows a vespagram example of the cube-root stack output as a function of slowness and arrival time relative to S2KS, with the small moveout curvature effects corrected. The observed dp^{3-2} and dp^{4-2} (red circles) closely agree with theoretical predictions by KHOMC (Table 3), which are shown by red stars in the figure. The RMS residuals computed for the Fiji-Tonga and Argentina events using the outer core models (PREM, IASP91, KOCTI, AK135, SP6, and Tanaka-1) show that the least residual is obtained for KHOMC (Fig. 5b). The RMS residual is less than 0.03 s/° for KHOMC (Fig. 5b), and dp^{3-2} for the majority of the events, which agree with KHOMC within 0.02 s/° (Table 3). The residuals for KHOMC of dp^{3-2} and dp^{4-2} are slightly improved in comparison to PREM, while no such dp^{m-n} improvement is seen for the other models. The small discrepancy of the observed dp^{3-2} and dp^{4-2}, with respect to PREM, justifies the usage of PREM as the reference model for stripping the mantle contributions from the observed distance ranges and travel times in the τ-p inversion that resulted in KHOMC (HK2010; KH2013). While the primary information about the core V_p structure is contained in the differential S*m*KS travel times, as shown in parameter tests (KH2013), the measured dp^{3-2} and dp^{4-2} data not only indicate the validity of our travel time analyses but also further support the validity of KHOMC.

S*m*KS differential times of other regions

Observations of dt^{3-2}

KHOMC was built by using the Tonga-Fiji data set that samples rather limited areas of the CMB, mostly beneath western Pacific and Siberia. KH2013 showed that the S*m*KS differential travel times of the Argentina to Japan data set are consistent with KHOMC, even though they sample entirely different parts of the CMB. In this study, we compile the dt^{3-2} measurements for additional pairs of event and large-scale array that sample a much larger portion of the CMB. We determine the anomalies of dt^{3-2} for several large-scale arrays (Japan, US, Australia, Alaska, Africa, South America, and Southeast Asia; Fig. 6a) using the same processing. The ray paths cover a reasonably large part of the outer core (Fig. 6a).

A striking feature of the result is that the dt^{3-2} observations based on the large-scale array processing are quite well matched by KHOMC (Fig. 6b). On the other hand, the dt^{3-2} values measured for individual stations (Souriau et al. 2003) show a much larger scatter than the array measurements (Fig. 6b), which suggests that measuring dt^{3-2} using large-scale array data significantly ameliorates the heterogeneous mantle structure effects. Another notable feature is that the array measurements fall approximately in the middle of the range of individual station measurements (Figure six b; Souriau et al. 2003), which also suggests that the array measurement of this study has successfully represented the overall core structure. The total residual of the array measurements is computed for KHOMC and for other outer core V_p models (IASP91, Tanaka-1, Tanaka-3, ak135, SP6, and PREM), and the least

Table 3 Differential slowness (dp^{3-2} and dp^{4-2},s/°)

Event	Distance Δ_0	dp^{3-2} (s/°)	KHOMC	Residual	dp^{4-2} (s/°)	KHOMC	Residual
FEV1	154.0	1.16	1.16	0.0	1.62	1.61	0.01
FEV2	154.0	1.20	1.16	0.04	1.65	1.61	0.04
FEV3	152.5	1.15	1.13	0.02	1.60	1.57	0.03
FEV4	152.0	1.14	1.13	0.01	1.59	1.57	0.02
FEV6	153.5	1.19	1.18	0.01	1.65	1.65	0.00
FEV12	150.0	1.12	1.11	0.01	1.56	1.53	0.03
KEV1	155.0	1.20	1.16	0.04	1.64	1.62	0.02
AEV2	157.8	1.19	1.21	−0.02	1.70	1.69	0.01
AEV3	162.6	1.20	1.18	0.02	1.65	1.65	0.00
AEV4	160.0	1.30	1.23	0.07	1.77	1.73	0.04
AEV5	167.8	1.30	1.28	0.02	1.80	1.77	0.02

The corresponding values calculated for KHOMC and the residuals of the observed values from the KHOMC predictions are also shown. Alignment is at the center distance of the array

misfit is obtained for KHOMC (Fig. 6c). As mentioned previously, we note that KHOMC definitely gives a better fit than the τ-p model based on IASP91 (KOCTI) for larger distances. These observations indicate that the mantle effects on dt^{3-2} are of secondary importance and that the essential features of KHOMC relative to PREM reflect the structure of the core.

Observations of dt^{4-3} and dt^{5-4}

The ray paths for which dt^{4-3} can be determined by using large-scale array data are geographically more restricted around Pacific than in the case of dt^{3-2} but still sample a reasonably broad portion of the CMB (Fig. 7a). The measured dt^{4-3} values fall in the middle of individual station measurements (Garnero et al. 1993) and are well consistent with KHOMC (Fig. 7b). Among the V_p models considered (Fig. 7d), the dt^{4-3} observations are best matched by KOCTI, but the data set (especially for category A) is explained almost equally well by KHOMC; the dt^{4-3} data set is not useful for discriminating between the two models. The other models (IASP91, Tanaka-1, Tanaka-3, AK135, and SP6) give significantly poorer fits when compared with KHOMC and KOCTI.

The dt^{5-4} data set is matched well by some of the models considered, KHOMC, PREM, IASP91, and KOCTI (Fig. 7c), so that it is not crucial to discriminate between the models. Nevertheless, it clearly refutes the class of models that have a strong V_p reduction in a thin layer at the top of the outer core, such as Tanaka-1, Tanaka-3, and that of Garnero et al. (1993). These models were built without using dt^{5-4} and were aimed to match mainly dt^{3-2}, which means that the amount of V_p anomaly relative to PREM across the top several hundred kilometers of the outer core can be well predicted by these models. The mismatch between these models with the observed dt^{5-4} means that the V_p anomaly relative to PREM needs to be distributed over a broader depth range than those in the models. This also indicates that the V_p gradient near the top of the core is not extremely anomalous compared to PREM (Fig. 3). The inference is further supported by the good match of the observed S6KS waveforms relative to S5KS by KHOMC (KH2013); the V_p gradient near the top of the core is tightly constrained by our data set.

We emphasize again that KHOMC was constructed by using the Fiji-Tonga to Europe data set alone, yet the observations of dt^{4-3} and dt^{5-4} for different regions can be matched by the same model quite well. The S*m*KS data we used, therefore, should primarily reflect the outer core structure.

Anomalous outermost core in terms of V_p gradient

The most important feature of our V_p models (KHOMC and KOCGA) is the presence of marked radial change in the V_p gradient, $V'_p = dVp/dr$; the outermost core of KHOMC and KOCGA is essentially characterized by two distinctive layers with different V'_p. We parameterize the V_p structure of the outermost 700 km of the core with two layers that have constant V'_p and compute the misfits of dt^{3-2}, dt^{4-3}, and dt^{5-4} for the Fiji-Tonga and Argentina data sets (KH2013).

The minimum misfit in this modeling is obtained for the V_p value at the CMB near that of KHOMC (−0.35 km/s with respect to PREM). For this case, the obtained V'_p value of the shallower layer approximately agrees with the mean values of V'_p of the shallower 300 km for KHOMC and KOCGA (Fig. 8), which indicates that the mean V_p gradient of the shallower layer is well constrained (Fig. 8) by the presence of additional different S*m*KS waves passing through it. Although the lower layer gradient is rather poorly constrained, the significant difference in the values of V'_p anomalies relative to PREM between the two layers is robust; the anomaly of V'_p with respect to PREM

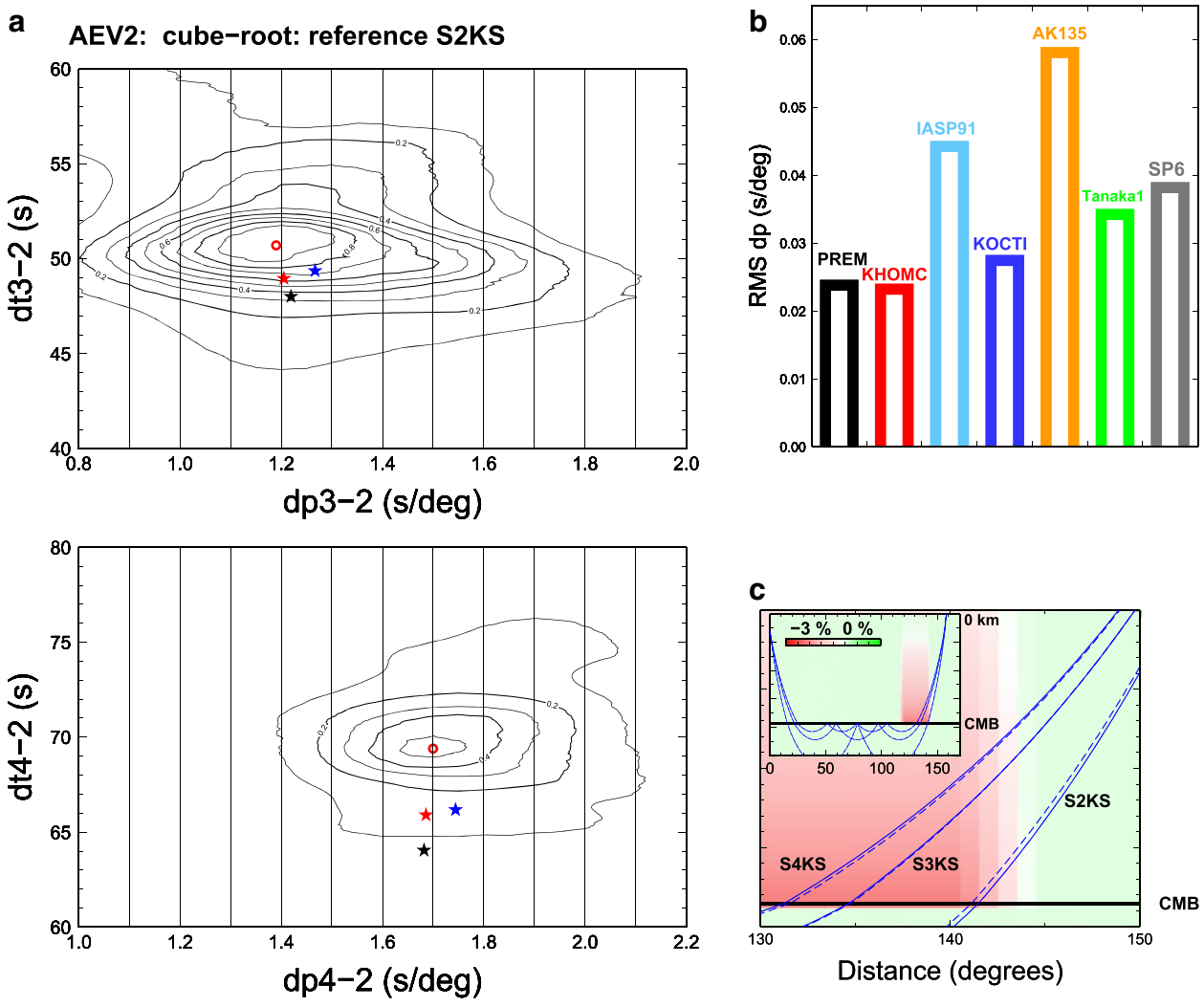

Fig. 5 Slowness measurements. (**a**) The observed differential slownesses, dp^{3-2} (top) and dp^{4-2} (bottom). Horizontal axis is slowness (in $s/°$) as a function of time after the arrival of S2KS (vertical axis). Red, blue, and black stars indicate the predictions from KHOMC, IASP91, and PREM, respectively. (**b**) RMS misfits of dp^{3-2} and dp^{4-2} in $s/°$ for different outer core models. The difference in the misfit between Takana-1 and Tanaka-3 is small. (**c**) An artificial model of 2D V_s heterogeneity localized near the bottom of the mantle receiver-side structure and the ray paths of S2KS, S3KS, and S4KS, after the Earth-flattening transformation. Dashed and solid blue rays are those for the unperturbed and perturbed Earth models, respectively. Inset shows the entire paths, while the rays near the receiver side CMB are focused below. The V_s anomaly is shown with color scale

(dV'_p=$dVp/dr_{profile}$ - dVp/dr_{PREM}) is much larger in the shallower part of the depth range considered than below it (Fig. 8). Accordingly, the V'_p of the shallower 300 km of the outer core is steeper than PREM by about 0.0001 (1/s), while that of the deeper part is closer to that of PREM. The number anomalies of V'_p (relative to PREM) obtained for the Genetic algorithms (KOCGA) is 0.00012 (1/s) for the upper ∼300 km of the core, while that is −0.00002 (1/s) for the deeper part (300 to 700 km from the CMB).

The V_p gradient and the pressure derivative of bulk modulus ($K' = dK_s/dP$) are interrelated, and the principal feature of KHOMC indicates a substantial radial variation in K' within the uppermost 700 km of the outer core. By using the equation, $V'_p = -g(2V_p)^{-1}(K' - 1)$, K' can be computed from V_p . We find that the K' value of the outermost 300 km of the core is nearly 3.7, which is larger than that of the deeper core by about 0.2 (Butler and Anderson 1978). The estimated anomaly of K' for the upper 300 to 400 km of the outer core amounts to a nearly 5 % radial anomaly, which is more than an order of magnitude larger than the V_p anomaly itself.

Discussion

Effects of receiver-side mantle

Our previous studies have shown that large-scale array analyses adequately extract differential SmKS travel time

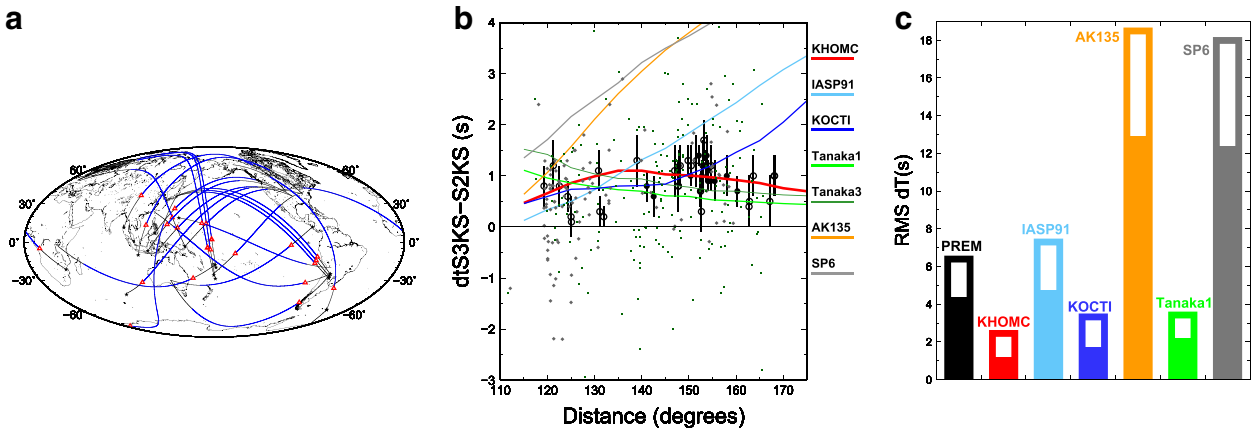

Fig. 6 Globally measured dt^{3-2} values. (**a**) Ray paths corresponding to the measured dt^{3-2}. Stars and red triangles show the epicenters and source side CMB entry points of S3KS. Blue portions of the ray paths indicate the segments within the outer core. For the events at Tonga-Fiji and Kermadec, only selected events and ray paths are plotted in order to prevent the figure from becoming excessively cluttered. (**b**) Measured dt^{3-2} for other large-scale arrays converted to a hypothetical focal depth of 500 km. The dt^{3-2} values predicted by global outer core models are shown with lines. The measured dt^{3-2} are shown by circles with error bars. Filled symbols show the data of category A, while open symbols are of category B (Table 2). The observed dt^{3-2} values are explained quite well by KHOMC (red line). Superimposed are the individual station-based dt^{3-2} data converted to 500 km focal depth (large diamonds) (courtesy of A. Souriau). Smaller squares are other dt^{3-2} measurements made for individual stations taken from Souriau et al. (2003) without depth corrections. (**c**) Total residuals, defined as the square root of the squared sum of the residuals of dt^{3-2} for different outer core models. Filled portions are the misfits for the category A data alone. The colors used for the models correspond to those in (**b**)

anomalies representative to the array as a whole (HK2010; KH2013). The receiver-side CMB piercing points for the Tonga-Fiji events scatter widely beneath Europe (HK2010; KH2013), making it difficult to envisage a receiver-side mantle heterogeneity which causes a systematic anomaly of S*m*KS differential travel times across the entire array.

Nevertheless, we attempt to conservatively evaluate the effects of mantle heterogeneity on the dt^{3-2} and dt^{4-3} measurements, by focusing on the observation of very

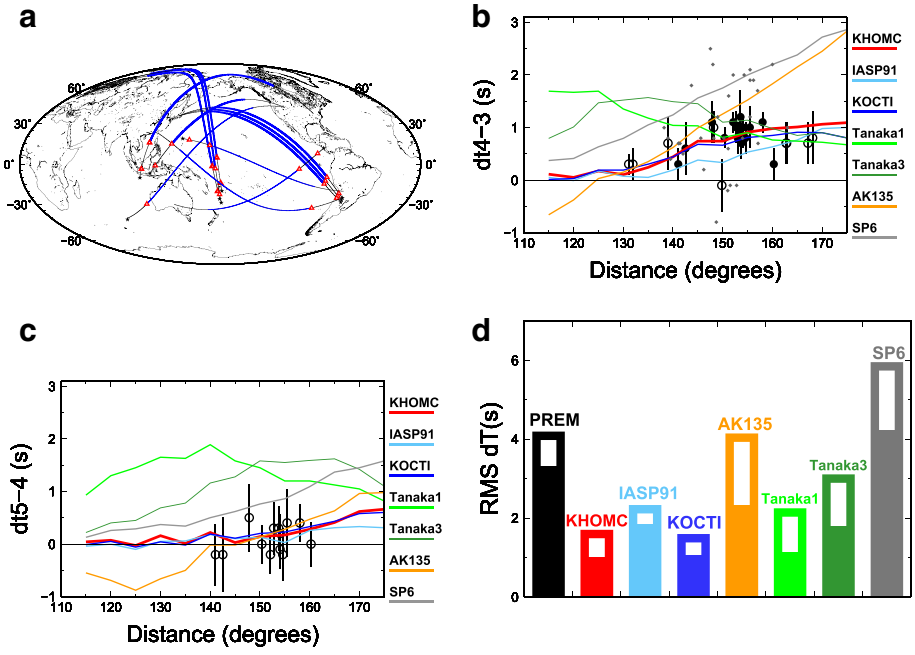

Fig. 7 Globally measured dt^{4-3} and dt^{5-4} values. (**a**) Ray paths for the dt^{4-3} and dt^{4-3} measurements. The CMB piercing points are of S4KS. Thick lines show the ray paths for which both dt^{4-3} and dt^{5-4} are measured, while thin lines show the ray paths for which only dt^{4-3} is measured. Other details are the same as Fig. 6a. (**b**) Measured dt^{4-3}. Details are the same as in Fig. 6b. (**c**) Measured dt^{5-4}. Details are the same as in Fig. 6b. (**d**) Total residuals for dt^{4-3}. Details are the same as in Fig. 6c

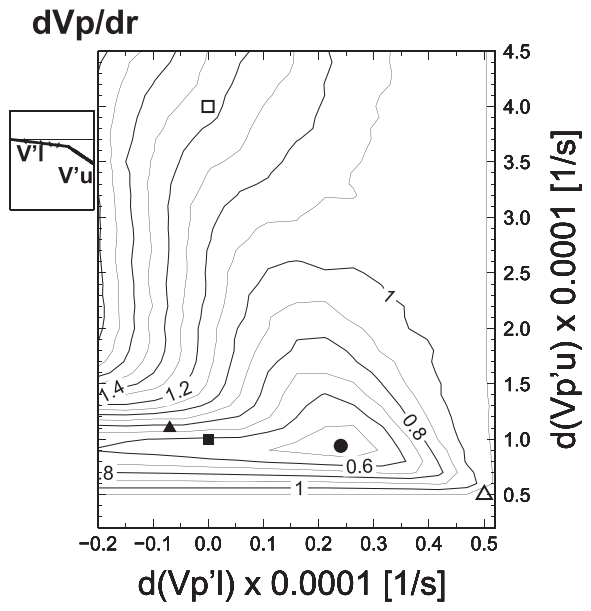

Fig. 8 V_p gradient with respect to PREM for a two-layer outermost core. Contour plot of total residual (in seconds) of dt^{3-2}, dt^{4-3}, and dt^{5-3} for the two-layered outer core model for the case of V_p at the CMB of 8.03 km/s, which give the least residual. The input data are as follows: $dt^{3-2} = 1.0$, $dt^{4-3} = 1.0$, and $dt^{5-3} = 0.9$ for 154° and h = 500 km representing typical values of the Fiji-Tonga data set; and $dt^{3-2} = 0.7$, $dt^{4-3} = 0.9$, and $dt^{5-3} = 0.9$, 162° and h = 590 km, representative of the Argentina data set. The deviation of V'_p from PREM ($dVp/dr_{profile}$ - dVp/dr_{PREM}) for the shallower part of the depth range (vertical axis) and the that of the deeper layer (horizontal axis). The points approximately representing KHOMC, KOCGA, IASP91, and Tanaka-1 are shown by a solid square, solid triangle, open triangle, and open square, respectively

small residuals of differential slownesses dp^{3-2} and dp^{4-2} described above from KHOMC (Fig. 5b). The observations indicate that the relative arrival angles of the different S*m*KS waves are barely anomalous and the rays of the S*m*KS waves are not substantially bent with respect to each other. A dp^{3-2} anomaly of 0.02 s/° or less for the majority of the events (Table 3) corresponds to the anomaly in the separation of S3KS and S2KS piercing points at the CMB of the receiver side by less than 5 km.

We argue that a differential travel time anomaly (dt^{3-2} and dt^{4-3}) as large as those observed would need to be accompanied by a large anomaly in the relative direction of ray arrivals at the receivers when the anomaly is caused by the mantle heterogeneity beneath the receiver (Fig. 5c). For a low V_s heterogeneity to cause a dt^{3-2} anomaly exceeding 1 s across the array, S2KS waves would need to more effectively avoid the heterogeneous body compared to S3KS (e.g., Garnero and Helmberger 1995). This effect on the ray angle deviations was evaluated by ray tracing experiments. The typical dominant period of S2KS and S3KS is nearly 10 s, and dt^{3-2} values measured for 3 s high-pass filtered seismograms of three Tonga-Fiji events (FEV2, FEV3, and FEV4) and two Argentina events (AEV2 and AEV4) agree with those for the original broadband seismograms within 0.3 s. They agree within 0.1 s for two of the Fiji events. This result confirms the utility of conducting theoretical ray estimations on dt^{3-2} to identify possible mantle heterogeneity effects. Therefore, we will next consider a test case involving an artificially strong and sharp-edged 2D low-V_s anomaly that extends about 1000 km from the CMB with a V_s anomaly that is a maximum 3 % slower in the receiver side of the lowermost mantle (Fig. 5c). The dt^{3-2} and dt^{4-3} anomalies at approximately 150° are 1.8 s and 0.8 s, respectively, which are comparable to the observations. The relative slownesses, dp^{3-2} and dp^{4-2}, are 0.10 and 0.14 s/°, respectively, which are nearly five times larger than the observations. Accordingly, the rays of S3KS and S2KS, as well as those of S4KS and S2KS, bend relatively by approximately 25 km at the CMB. The observed minute anomalies in dp^{3-2} and dp^{4-2} indicate that the receiver-side piercing points are much less significantly bent than is required by this model. The maximum V_s anomaly needs to be as low as 0.6 % in order to match the observed dp^{3-2} and dp^{4-2}, which sets the upper bounds on the allowable biases of dt^{3-2} and dt^{4-3} due to the receiver-side heterogeneity to much less than 0.4 s and 0.2 s, respectively.

Effects of source-side mantle

A source-side lower mantle structure that is capable of causing a dt^{3-2} anomaly of ∼1 s across the entire European array would need to be laterally much larger than 200 km (KH2013). For the source-side mantle sampled by the Fiji-Tonga data set, the V_s structure in the D″ of very large scale (≥3000km) beneath the north of Vanuatu seems to have been resolved moderately well by global seismic tomography (e.g., Lekic et al. 2012). Therefore, it would appear worthwhile to check whether V_s heterogeneity of a larger scale in the source side deep mantle accounts for a significant portion of the S*m*KS differential travel time anomalies.

We focus on five Fiji-Tonga events that are located from 300 to 1000 km laterally separately from each other (Fig. 9a) and for which high quality S2KS, S3KS, and S4KS have been observed (Table 2). The five events sample the CMB regions that are shifted systematically by 200 to 600 km; each event covers a CMB area of ∼1000 km by 300 km (Fig. 9b). Effects of D″ should be most significant for dt^{3-2}, since S2KS and S3KS have larger CMB piercing point separations; dt^{4-3} should be less sensitive to heterogeneity in D″ as the separations of the CMB entry points between S3KS and S4KS are less than half of dt^{3-2}.

We find that the dt^{3-2} anomalies for the five events are nearly uniform and are excellently matched by KHOMC (Fig. 10a), which is also the case for dt^{4-3} (Fig. 10b). The

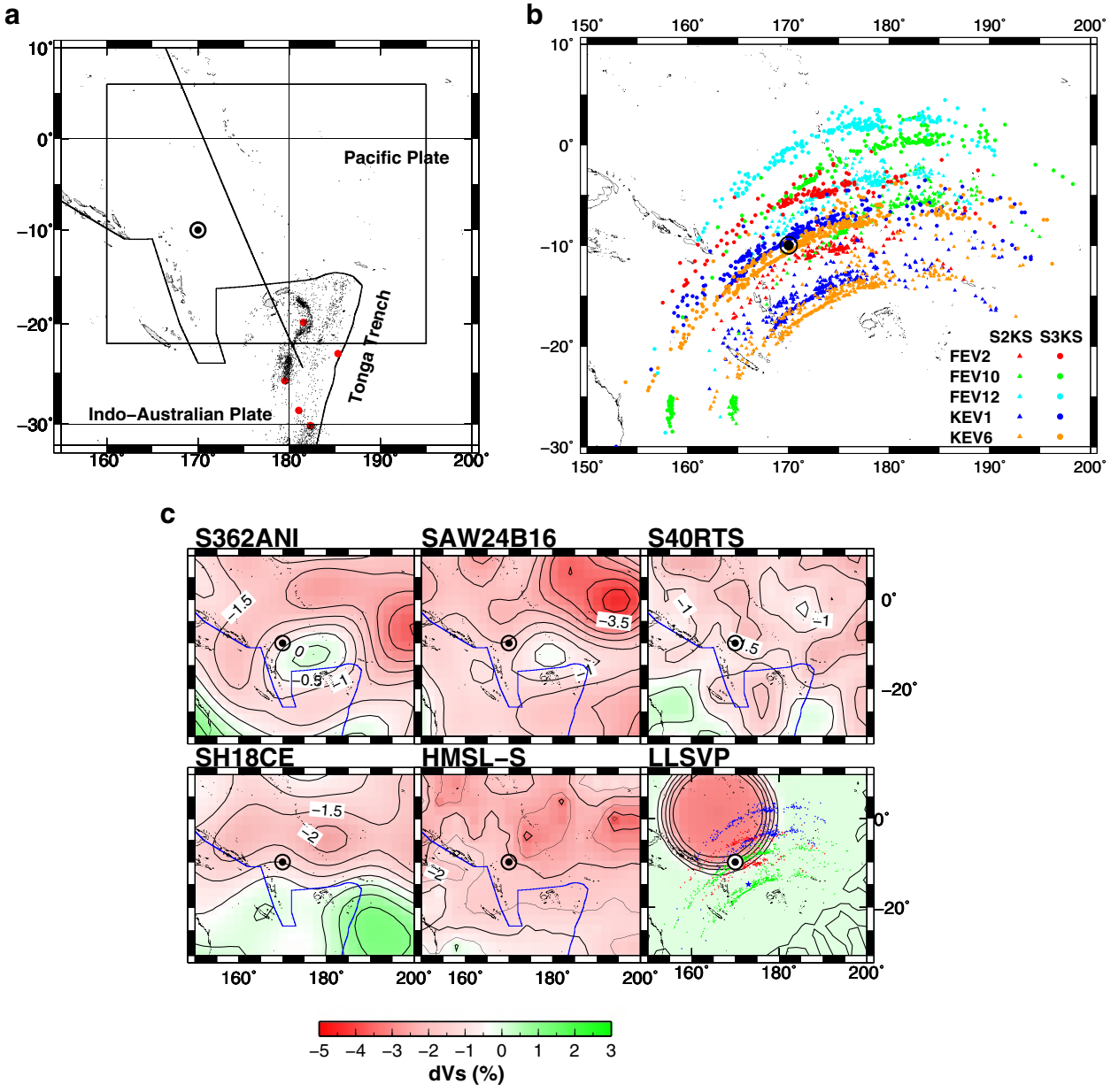

Fig. 9 Tonga-Fiji events. (**a**) Locations of the five events, FEV2, FEV10, FEV12, KEV1, and KEV6. (**b**) CMB piercing points for S2KS and S3KS for the four events. Triangles and circles show the core entry points of S2KS and S3KS for each event, respectively. The large black circles are drawn to mark a reference point referred as below. (**c**) The V_s anomalies in the D″ beneath Vanuatu around the CMB piercing points of the Fiji-Tonga data set for the five tomography models: SAW24B16 (Megnin and Romanowicz 2000), S362ANI (Kustowski et al. 2008), HMSL (Houser et al. 2008), SH18CE (Takeuchi 2007), and S40RTS (Ritsema et al. 2011). The V_s anomalies are shown with color code and contours. The large black circles show the reference point. Bottom right panel shows a model with an extreme and sharp-edged anomaly, like LLSVP. The piercing points of S2KS and S3KS for three of the five events are shown in this panel only

V_s models produced by global tomography appear to provide moderately reliable images of the deepest ~200 km of the mantle (essentially corresponding to D″) of this region, at least for wavelength features exceeding 2000 km. According to the V_s models for the 2800 km depth of five different tomography studies (Fig. 9c), despite considerable differences in detail, the presence of 1 to 3 % low V_s in the D″ of the northern half of the study area seems to be commonly resolved. On the other hand, the depth extent of such anomalies are very poorly constrained, and 2500 km depth tomography images show only insignificant anomalies that differ substantially from model to model. Therefore, we only deem the heterogeneity in the D″ to be significant and evaluate its effects on S*m*KS travel

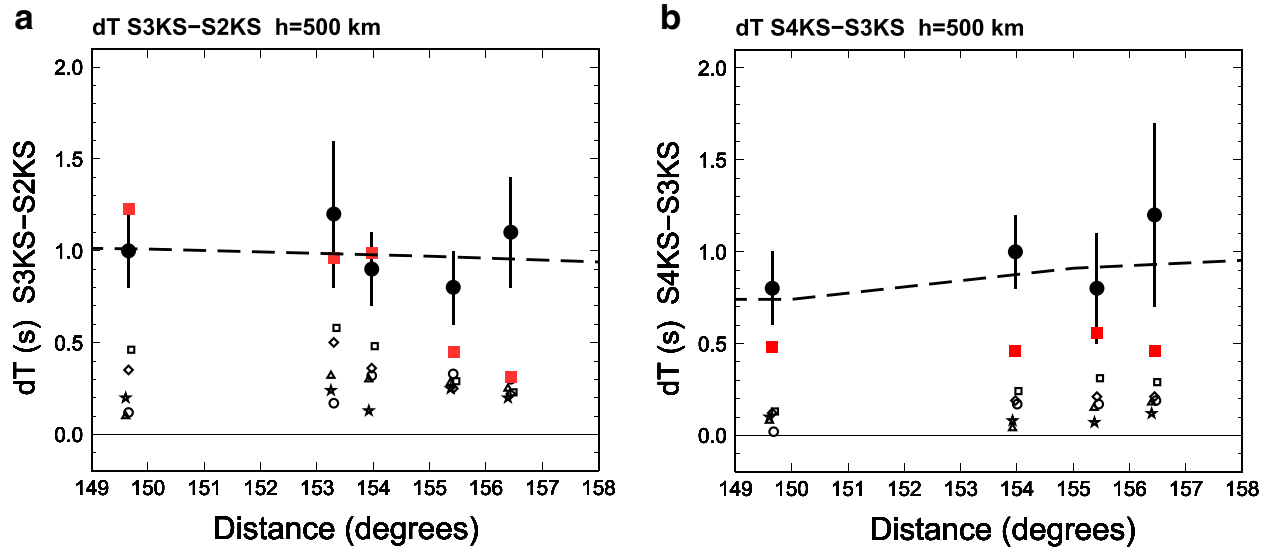

Fig. 10 Effects of source side D″. (**a**) Symbols with error bars show the anomalies with respect to PREM of dt^{3-2} measured for the five events in Fig. 9a as a function of array center distance from the epicenters. Small symbols are the predicted effects of the D″ heterogeneity for five different tomography models (those in Fig. 9c). Large red squares show the anomalies of dt^{3-2} predicted by the artificial lower mantle heterogeneity model shown in the bottom right panel of Fig. 9c. (**b**) Same as (**a**) for dt^{4-3}

times, rather than attempting to make corrections on the S*m*KS travel times for the effects of mantle heterogeneity. Ray theoretical travel times computations show that the tomography-derived structures of D″ could systematically affect the anomalies of dt^{3-2} values by 0.3 s on average (Fig. 10a), while the dt^{4-3} anomalies by 0.2 s (Fig. 10b). These effects may cause small biases to the core models but do not alter them significantly.

If an extreme but currently unresolved heterogeneity that is analogous to LLSVP with a sharp edge exists near the source side CMB entry points of S*m*KS, it might cause dt^{3-2} and dt^{4-3} anomalies of the observed magnitude. As an example of such a scenario, we will next consider a simplified but significantly exaggerated model that has a qualitative resemblance with the tomographic V_s anomalies of the D″ (Fig. 9c) and evaluate the effects of the extreme lower mantle heterogeneity. The model that we will consider has an axisymmetrical tabular-shaped low V_s heterogeneity that has a maximum anomaly of 3.5 % at the CMB and that exponentially decays upward with a scale height of 500 km (Fig. 9c, bottom right). Theoretical dt^{3-2} and dt^{4-3} for this model are computed by ray theory (Fig. 10a, b). The values of dt^{3-2} can be as large as the observed values depending on the epicentral distance. However, there should be a clear trend in dt^{3-2} with the epicentral distance by about 1 s, which is entirely different from the observed dt^{3-2} trend. The relative magnitudes of dt^{3-2} and dt^{4-3} are also grossly inconsistent with the observation. The heterogeneity model significantly underestimates as a dt^{4-3} value that is less than half of the observations, mostly because of the smaller separation of the CMB piercing points (Fig. 10a). Although this demonstrates only just one example, the basic feature of V_s structures that potentially cause dt^{3-2} anomalies as large as the observed values should be more or less the same. S2KS more effectively avoids the low V_s body than S3KS. Simplified mantle heterogeneity models resembling tomography images, no matter how pronounced and sharp they are, have difficulty matching the observed dt^{3-2} and dt^{4-3} of the Tonga-Fiji data set. Therefore, we conclude that an unresolved lower mantle heterogeneity is unlikely to be the predominant cause of the observed S*m*KS anomalies, and estimate its effects on dt^{3-2} and dt^{4-3} values based on the current tomography models to be less than 0.3 s and 0.2 s, respectively.

Interpretations in terms of the composition of the core

As suggested by high estimates of liquid iron thermal conductivity, a thermally stratified layer in the neighborhood of 100 km thick might exist in the outermost core (Pozzo et al. 2012). However, a more recent numerical estimate of the electrical conductivity of iron under the Earth's core conditions has negated the thermal stratification requirement (Zhang et al. 2015). If the stratified layer is nearly 300 km thick, as estimated in this study, the maximum temperature excess over the adiabat at the CMB would be about 300 K. Recent ab initio calculations of liquid and solid iron show that the bulk sound speeds of iron are mostly independent of temperature (Ichikawa et al. 2014; Vocadlo et al. 2009). Therefore, the observed V_p and V_p' anomalies in the uppermost 300 km of the outer core cannot be of thermal origin and should primarily reflect

compositional heterogeneity. Since the effective dK/dP in the layer is larger than the bulk of the core, if the light elements diffuse downward from the CMB (and thus have concentrations decreasing with depth), the addition of the light elements must decrease not only the density of the liquid iron alloy but also its bulk modulus. According to recent ab initio calculations of liquid iron-alloy under the core conditions (Badro et al. 2014), these requirements are satisfied. However, the same calculations show that including light elements increases V_p . Thus, it seems that matching the observed V_p value at the CMB cannot be done by simply by adding light elements, even though the effects of non-ideal mixing in the iron alloy (which might not be adequately modeled in the simulations) might still play a role in reducing V_p (Helffrich 2012).

The estimated thickness of the compositionally stratified layer (∼300 km) cannot be interpreted via a straightforward process. If the stratified layer evolved from the CMB through the diffusion of light elements, the thickness of the layer is essentially determined by the diffusion coefficient of the core liquid. The mass diffusivity of liquid iron under core conditions is thought to be reasonably well constrained (Koci et al. 2007; Pozzo et al. 2012; Helffrich 2014), and the expected thickness is no more than 80 km (Buffett and Seagle 2010; Helffrich and Kaneshima 2013). Helffrich (2014) suggests that the presence of a thick layer is a feature of the Earth's core that was formed at the time of the putative giant impact.

While the V_p profile of the top 700 km of the core is adequately represented by two layers with nearly constant radial V_p profile gradients, there is certainly room for the profile to be optimized with some physically plausible constraints, such as the diffusion profile of light elements (Helffrich 2014). However, the revelation of detailed features of the V_p profile is somewhat more difficult due to the presence of mantle effects that have secondary importance. Based on the lack of corresponding anomalies in the waveforms, a sharp interface with a large V_p jump at the bottom of the shallower layer near the depth of 300 km is unlikely to exist, but the presence of a weak jump cannot be ruled out. If light elements diffuse from the CMB, and if double diffusion takes place to form the stratified layer, a succession of thin homogeneous layers might occur near the bottom of the stratified layer (e.g., Buffett and Seagle 2010). In such cases, scattering of seismic energy might occur near the bottom of the layer, depending on the contrasts in the elastic properties between the materials enriched and depleted in light elements. A search for such scattering waves might reveal further details about the enigmatic region of deep Earth. On the other hand, the very top of the core is obviously another locality where an anomalous structure is possible. The existence of a thin and anomalously high V_p and low density layer at the top of the core (Helffrich and Kaneshima 2004) is not supported, if the layer thickness exceeds 10 km or so, by a good fit of the waveforms S6KS to KHOMC (KH2013). Nevertheless, a thinner layer might exist.

Conclusions

The differential travels between SmKS measured by analyzing large-scale broadband seismometer arrays are shown to predominantly reflect the V_p structure of the outermost outer core. The combination of dt^{3-2}, dt^{4-3}, and dt^{5-4} anomalies restrict permissible V_p models within a narrow range. There is a significant radial change in gradient of V_p at the depth about 300 km below the CMB. The gradient of the shallower layer corresponds to an effective change in dK_s/dP by about 0.2, which is too large to be attributed to thermal effects alone, and requires compositional stratification.

Abbreviations

LLSVP, Large low shear velocity province; HK2010, Helffrich and Kaneshima (2010); KH2013, Kaneshima and Helffrich (2013).

Competing interests

The authors declare that they have no competing interests.

Authors' contributions

SK performed the analyses and wrote the manuscript. TM prepared for the Hi-net tilt-meter data. Both authors read and approved the final manuscript.

Acknowledgements

This study owes a great deal to the management of waveform data by IRIS DMC, the NDIC's F-net in Japan, the J-Array Data Center, the Taiwan Data Center, and the ORPHEUS Data Center in Europe. Generic Mapping Tools (GMT) (Wessel and Smith 1995) were used for drawing all of the figures. Appreciation is extended to A. Souriau and G. Helffrich for providing individual S3KS-S2KS travel time measurement data. Thanks are also extended to George Helffrich who kindly checked our manuscript, and J. Ritsema who generously provided data from his tomography model. T. Tsuchiya is thanked for his enlightening discussions, and the comments and suggestions of Satoru Tanaka and the two anonymous reviewers were very helpful for improving the manuscript.

Author details

[1]Department of Earth and Planetary Science, Kyushu University, Hakozaki, Higashi-ku, 812-8581 Fukuoka, Fukuoka, Japan. [2]National Research Institute for Earth Science and Disaster Prevention, 3–1 Tennodai, 305-0006 Tsukuba, Japan.

Received: 4 January 2015 Accepted: 14 May 2015
Published online: 24 June 2015

References

Alexandrakis C, Eaton DW (2010) Precise seismic-wave velocity atop Earth's core: No evidence for outer-core stratification. Phys Earth Planet Inter 180:59–65

Badro J, Cote AS, Brodholt JP (2014) A seismologically consistent compositional model of Earth's core. Proc Nat Acad Sci 111:7542–7545

Buffett BA, Seagle CT (2010) Stratification of the top of the core due to chemical interactions with the mantle. J Geophys Res 115. doi:10.1029/2009JB006751

Butler R, Anderson DL (1978) Equation of state fits to the lower mantle and outer core. Phys Earth Planet Inter 17:147–162

Choy G (1977) Theoretical seismograms of core phases calculated by a frequency-dependent full wave theory, and their interpretation. Geophys J Astr Soc 51:275–311

Dziewonski A, Anderson DL (1981) Preliminary reference Earth model. Phys Earth Planet Inter 25:297–356

Eaton DW, Kendall J-M (2006) Improving seismic resolution of outermost core structure by multichannel analysis and deconvolution of broadband SmKS phases. Phys Earth Planet Inter 155:104–119
Garmany J, Orcutt JA, Parker RL (1979) Travel time inversion: a geometrical approach. J Geophys Res 84:3615–3622
Garnero EJ, Helmberger DV (1995) On seismic resolution of lateral heterogeneity in the Earth's outemost core. Phys Earth Planet Inter 88:117–130
Garnero EJ, Helmberger DV, Grand SP (1993) Constraining outermost core velocity with SmKS waves. Geophys. Res. Lett. 20:2463–2466
Helffrich G (2012) How light element addition can lower core liquid wave speeds. Geophys J Int 118:1065–1070
Helffrich, G (2014) Outer core compositional layering and constraints on core liquid transport properties. Earth Planet Sci Lett 391:256–262
Helffrich, G, Kaneshima S (2004) Seismological constraints on core composition from Fe-O-S liquid immiscibility. Science 306:2239–2242
Helffrich G, Kaneshima S (2010) Outer-core compositional stratification from observed core wave speed profiles. Nature 468:807–810
Helffrich G, Kaneshima S (2013) Cause and consequence of outer-core stratification. Phys Earth Planet Inter 223:2–7
Houser C, Masters G, Shearer P, Laske G (2008) Shear and compressional velocity models of the mantle from cluster analysis of long-period waveforms. Geophys J Int 174:195–212
Ichikawa H, Tsuchiya T, Tange Y (2014) The P-V-T equation of state and thermodynamic properties of liquid iron. J Geophys Res 119. doi:10.1002/2013JB010732
Kaneshima S, Helffrich G (2013) Vp structure of the outermost core derived from analyzing large-scale array data of SmKS waves. Geophys J Int 193:1537–1555
Kennett BLN, Engdahl ER (1991) Traveltimes for global earthquake location and phase identification. Geophys J Int 105:429–465
Kennett BLN, Engdahl ER, Buland R (1995) Constraints on seismic velocities in the Earth from traveltimes. Geophys J Int 126:108–124
Kind R (1979) Extensions of the reflectivity method for a buried source. J Geophys 45:373–380
Koci L, Belonoshko AB, Ahuja R (2007) Molecular dynamics calculation of liquid iron properties and adibatic temperature gradient in the Earth's outer core. Geophys J Int 168:890–894
Kustowski B, Ekstrom G, Dziewonski AM (2008) Anisotropic shear-wave velocity structure of the Earth's mantle. J Geophys Res 113:B06306
Lay T, Young C (1990) The stably-stratified outermost core revisited. Geophys. Res. Lett. 17:2001–2004
Lekic V, Cottaar S, Dziewonski AM, Romanowicz B (2012) Cluster analysis of global lower mantle tomography: a new structure and implications for chemical heterogeneity. Earth Planet Sci Lett 357-358:68–77
Mégnin C, Romanowicz B (2000) The shear velocity structure of the mantle from inversion of body, surface and higher modes waveforms. Geophys J Int 143:709–728
Morelli A, Dziewonski AM (1993) Body wave traveltimes and a spherically symmetric P- and S-wave velocity model. Geophys J Int 112:178–194
Obara K, Kasahara K, Hori S, Okada Y (2005) A densely distributed high sensitivity seismograph network in Japan: Hi-net by National Research Institute for Earth Science and Disaster Prevention. Rev Sci Intrum 76:021301
Pozzo M, Davies C, Gubbins D, Alfe D (2012) Thermal and electrical conductivity of iron at Earth's core conditions. Nature 485:355–358
Ritsema J, Deuss A, Heijst H, Woodhouse J (2011) S40RTS: a degree-40 shear-velocity model for the mantle from new Rayleigh wave dispersion, teleseismic traveltime and normal-mode splitting function measurements. Geophys J Int 184:1223–1236
Souriau A, Teste A, Chevrot S (2003) Is there any structure inside the liquid outer core? Goephys. Res. Lett. 30. doi:10.1029/2003GL017008
Takeuchi N (2007) Whole mantle SH velocity model constrained by waveform inversion based on 3D Born kernels. Geophys J Int 169:1153–1163
Tanaka S (2007) Possibility of a low P-wave velocity layer in the outermost core from global SmKS waveforms. Earth Planet Sci Lett 259:486–499
Vocadlo L, Dobson DP, Wood IG (2009) Ab initio calculations of the elasticity of hcp-Fe as a function of temperature at inner-core pressure. Earth Planet Sci Lett 288:534–538
Wang P, de Hoop MV, van der Hilst R (2008) Imaging the lowermost mantle (D") and the core-mantle boundary with SKKS coda waves. Geophys J Int 175:103–115
Wessel P, Smith WH (1995) New version of generic mapping tools. EOS Trans. AGU Electron. Suppl. Aug. 15
Yamanaka H, Ishida H (1995) Phase velocity inversion using genetic algorithms. J. Struct. Constr. Eng. AIJ 468:9–17
Zhang P, Cohen RE, Haule K (2015) Effects of electron correlations on transport properties of iron at Earth's core conditions. Nature 517:605–607